Mon. Not. R. Astron. Soc. **291,** 219–234 (1997)

On the nature of the dark mass in the centre of the Milky Way

R. Genzel, A. Eckart, T. Ott and F. Eisenhauer

Max-Planck-Institut für extraterrestrische Physik, Giessenbachstrasse, D-85740 Garching bei München, Germany

Accepted 1997 June 12. Received 1997 June 12; in original form 1997 April 9

ABSTRACT

We discuss constraints on the properties and nature of the dark mass concentration at the core of the Milky Way. We present 0.15-arcsec astrometric *K*-band maps in five epochs beween 1992 and 1996. From these we derive imposed stellar proper motions within 3 arcsec of the compact radio source Sgr A* whose infrared counterpart may have been detected, for the first time, in a deep image in 1996 June. We also report $\lambda/\Delta\lambda \sim 35$ speckle spectroscopy and show that several of the Sgr A* (infrared) cluster members are likely early-type stars of mass $\sim$15 to 20 $M_\odot$. All available checks, including a first comparison with high-resolution maps that are now becoming available from other groups, support our previous conclusion that there are several fast-moving stars ($\geq 10^3$ km s^{-1}) in the immediate vicinity (0.01 pc) of Sgr A*. From the stellar radial and proper motion data, we infer that a dark mass of $2.61\ (\pm 0.15_{\rm stat})(\pm 0.35_{\rm stat+sys}) \times 10^6\ M_\odot$ must reside within about one light-week of the compact radio source. Its density must be $2.2 \times 10^{12}\ M_\odot\ {\rm pc}^{-3}$ or greater. There is no stable configuration of normal stars, stellar remnants or substellar entities at that density. From an equipartition argument we infer that at least 5 per cent of the dark mass ($\geq 10^5\ M_\odot$) is associated with the compact radio source Sgr A* itself and is concentrated on a scale of less than 15 times the Schwarzschild radius of a 2.6×10^6-$M_\odot$ black hole. The corresponding density is $3 \times 10^{20}\ M_\odot\ {\rm pc}^{-3}$ or greater. If one accepts these arguments it is hard to escape the conclusion that there must be a massive black hole at the core of the Milky Way.

Key words: black hole physics – astrometry – celestial mechanics, stellar dynamics – Galaxy: centre – infrared: general.

1 INTRODUCTION

Do massive black holes exist in galactic nuclei? This question is of considerable importance for the understanding of active galactic nuclei (AGNs) and the evolution of galaxies. There are a number of excellent indirect indicators that the answer to the above question is most probably 'yes' (e.g. relativistic radio jets, variable hard X-ray and γ-ray emission in AGNs, very fast gas motions seen in optical and X-ray spectra: see Begelman, Blandford & Rees 1984; Osterbrock & Miller 1989; Tanaka et al. 1995). However, a direct proof of the massive black hole paradigm is still missing. The most unambiguous way to answer the question is through using knowledge of the dynamics of nuclear stars (or orbiting gas) provided that one can come close enough to the black hole candidate to exclude other forms of mass concentrations (see Kormendy & Richstone 1995 and references therein). At a distance of 8 kpc (1 arcsec $= 1.2 \times 10^{17}$ cm: Reid 1993) the Galactic Centre is a unique laboratory in which to search for a central mass concentration and investigate its spatial distribution on scales of ≤ 0.01 pc (for recent reviews, see Genzel, Hollenbach & Townes 1994, and Mezger, Duschl & Zylka 1996). This scale will not be reachable for a while by direct measurement in the more spectacular, albeit also much more distant, AGNs. Evidence for a dark (i.e. very large ratio of mass to luminosity) central mass concentration of $2–3 \times 10^6\ M_\odot$ at the core of the Milky Way from observations of the radial velocities of gas and stars has been steadily growing since the late 1970s (e.g. Wollman et al. 1977; Lacy et al. 1980; Serabyn & Lacy 1985; Genzel & Townes 1987; McGinn et al. 1989; Sellgren et al. 1990; Krabbe et al. 1995; Genzel et al. 1996; Haller et al. 1996).

From diffraction-limited *K*-band (2 μm) imaging with the 3.5-m New Technology Telescope (NTT) of the European Southern Observatory (ESO) over the last five years Eckart & Genzel (1966, 1977, hereafter EG) have recently

reported, for the first time, the detection of stellar proper motions. These proper motions are in excellent agreement with the radial velocity data and push the size limit of the central mass downward by about an order of magnitude. It is this jump in size-scale of the dark mass that now allows us to distinguish between different proposed forms of the central mass concentration (single-mass black hole versus various clusters of stellar or substellar remnants).

In this paper, we present an improved analysis of stellar proper motions in the central few arcsec along with a few considerations of the stability of various dark clusters. We also report the first speckle spectroscopy of the fast-moving stars in the immediate vicinity of Sgr A*. Together with an equipartition argument we are then able to set a very interesting lower limit on the mass of Sgr A* itself. As a useful reference for future high-resolution imagery we present astrometric *K*-band maps (also available via the MPE homepage).

2 OBSERVATIONS

2.1 Improved analysis of proper motion data near Sgr A*

We have described in our earlier papers the steps we have taken to obtain ~0.15 arcsec near-infrared images (Eckart et al. 1992, 1993, 1994, 1995), 10- to 20-mas precision, relative stellar positions and, from such data over several years, significant proper motions (EG). Briefly, during a given night we are taking many thousands of short-exposure frames (0.3- to 0.5-s integration time) at the NTT. The data from nights with very good seeing (0.4 to 0.8 arcsec) are then processed in the standard manner (dead-pixel correction, sky-subtraction, flat-fielding etc.). Next we co-add the 256^2 pixel frames (1 pixel = 25 to 50 mas) using the brightest pixel of a bright star in the 6.4 to 12.8 arcsec field (IRS7 or IRS16 NE) as a shift-and-add reference (for details see Christou 1991 and Eckart et al. 1994). This is followed by CLEANing the raw shift-and-add images with the Lucy–Richardson (Lucy 1974) algorithm, using IRS7/IRS16 NE as the deconvolution key. We finally re-convolve the resulting component maps with a Gaussian restoring beam, of FWHM near the diffraction limit of the telescope (0.13 arcsec at 2.2 μm).

Of obvious importance for the determination of the mass distribution via the stellar dynamics is the region immediately around the dynamic centre (~Sgr A*). Within about 1 arcsec of the compact radio source there appears to be a local concentration of fainter stars we have termed the Sgr A* (infrared) cluster (Eckart et al. 1995). It is here that EG found rapid structural changes that they interpreted as proper motions in excess of 10^3 km s^{-1}. Because of the important implications of the implied large motions very close to Sgr A*, and the technical difficulties in deriving significant motions in this crowded environment, we have reanalysed the data of EG by adding extra data in 1996 and including a good data set from the 1992.65 epoch. Compared with EG's analysis this approximately doubles the time baseline. However, our data from epochs earlier than 1994 April suffered from variable seeing conditions. In order to obtain a high-resolution image for the 1992 August epoch we selected the two very best sets of frames and processed them as described above. The resulting image is in very good agreement with the high-resolution images obtained for the later epochs. The time difference between the next high-resolution epoch in 1994 April is about 1.7 yr. This makes it difficult to identify source components in the southern part of the Sgr A* cluster, including sources S8 through S11. The identification of sources S1 through S7, with the exception of S3, however, is straightforward. The identifications we use are given in Fig. 1.

2.2 Astrometric maps

In Fig. 2 we present astrometric maps for all five epochs. The maps in Fig. 2 are labelled with positions relative to the best radio position of the radio source Sgr A* in the infrared rest frame (see Menten et al. 1997). In order to produce these maps we used the astrometric *K*-band image we published in Menten et al. (1997) as a reference. This image was placed on the same Very Large Array (VLA) radio reference frame as in Menten et al. via the *K*-band identification of five H_2O/SiO maser stars. Using 10 bright comparatively isolated stars in the central 3.5×3.5 arcsec^2 we matched offset, position angle and image scale of our best images of the individual epochs. The comparison of the 1995 data with the VLA radio data in Menten et al. (1997) resulted in a measurement accuracy for relative positions of better than 30 to 40 mas over ~20 arcsec. This corresponds to an error of about 6 mas across our 3.5×3.5 arcsec^2 field of view in Fig. 2. From our comparison of the positions of the 10 selected stars we estimate that an additional error in the relative alignment of images from different epochs is of approximately the same order of magnitude, so that the total error in relative alignment is about 8 mas. For a time difference of about 4 yr this corresponds to an error of about 50 km s^{-1} for proper motions directly read off by comparing the maps in Fig. 2. The result can in fact be checked by comparing the images that are furthest apart in time. Such a comparison visually reveals differences between the positions of all individual stars in the field. These differences correspond very well to the proper motions calculated by EG using a different algorithm to obtain the imaging parameters for each data set. These calculated motions have a higher precision since they include also second-order and mixed terms.

2.3 Speckle spectroscopy

We carried out speckle spectroscopic observations at resolving power $R = \lambda/\Delta\lambda = 35$ during NTT observing runs in 1996 April and June. The pointing was chosen such that the central part of the stellar cluster with IRS7 ($K = 6.7$), used as a structural calibrator, a featureless star (IRS29N), used as a spectral calibrator (Krabbe et al. 1995; Genzel et al. 1996) and the 1-arcsec diameter Sgr A* region were contained in each exposure. In order to obtain low-resolution *K*-band spectra we constructed an objective prism for the SHARP1 speckle camera (Hofmann et al. 1993) at the NTT. This additional optical device consists of two optically contacted prisms. One is made from BaF_2 and the other from Schott IRG9 glass. Mounted in front of the SHARP1 camera the two prisms have an on-axis net dispersion that gives full *K*-band spectra of 1.0-arcsec length in the image plane. This

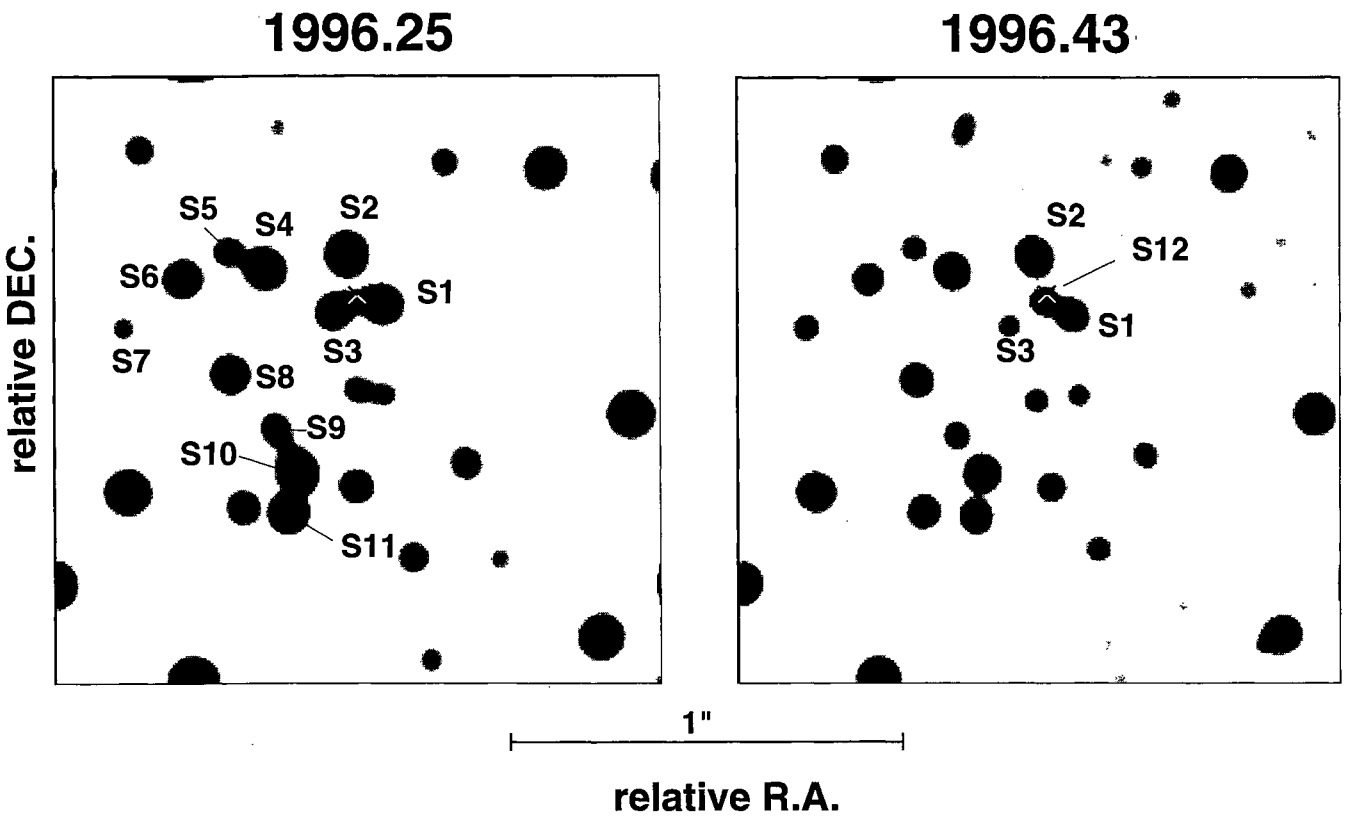

Figure 1. Grey-scale representations of deep, super-resolution K-band maps (0.07-arcsec FWHM) of the central 3×3 arcsec^2. The maps contain 3.7-h on-source integration in April (27 000 frames at 0.5-s integration time with 50-mas pixels) and 3.6-h (26 000 frames at 0.5-s and 50 mas) plus 1.1-h (8000 frames at 25 mas) in 1996 June. The 3σ noise floor is approximately at $m(K) \sim 17$. IRS7 was taken as the reference source. Marked in the 1996 June map are the identifications of sources listed in Table 1. The cross marks the position of the compact radio source Sgr A*.

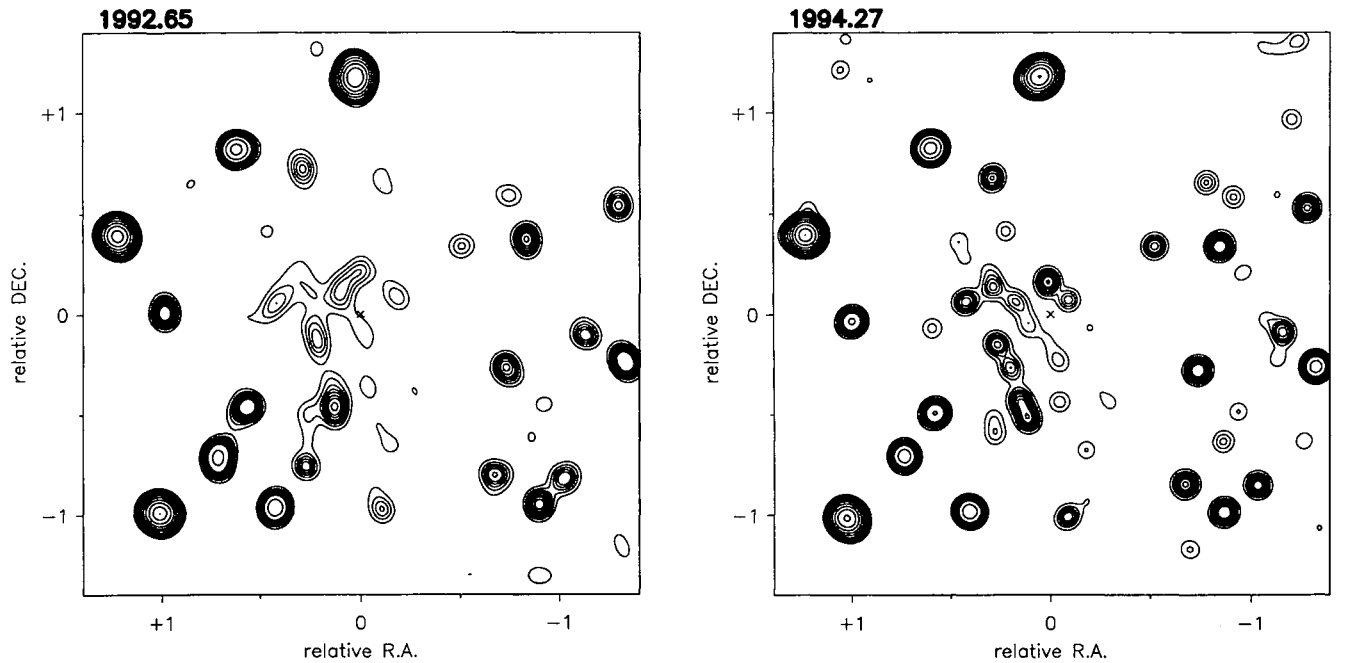

Figure 2. Astrometric 0.15-arcsec K-band maps of all five epochs (see text for details). Electronic versions of these maps can be obtained via the MPE homepage. The cross at the centre of all maps marks the position of the compact radio source Sgr A*. The alignment of the radio and near-infrared reference frames has been carried out as in Menten et al. (1997). The 1σ positional uncertainty of this alignment is ± 30 mas. In our maps positions relative to Sgr A* are given in arcsec. Contours are 0.2, 0.4, 0.6, 0.8, 1, 1.3, 1.6, 2.4, 8, 16, 32, 64 and 100 per cent of the peak K magnitude per beam (~ 9.4). To include the faint source S3 in the 1994.42 map we plotted, in addition, the 0.1 and 0.17 per cent levels.

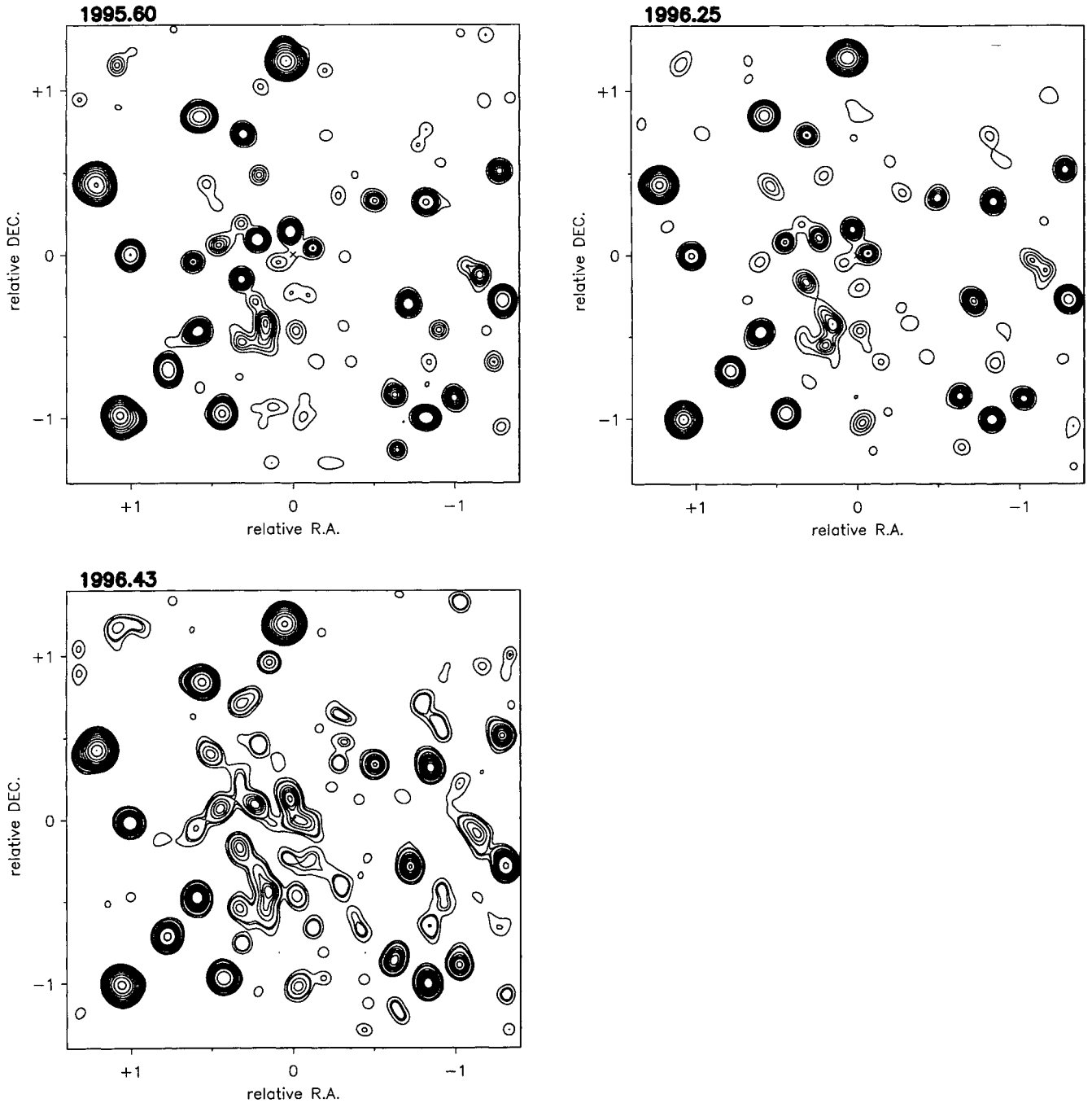

Figure 2 – *continued*

dispersion was chosen on purpose in order to minimize confusion problems in the highly crowded area surrounding the compact radio source Sgr A*. The spectral range is limited by the *K*-band filter (1.95–2.40 μm) inside the camera. We focused the images by optimizing the short-exposure image contrast. Spectrally dispersed speckle interferograms were then recorded with exposure times of 0.5 s. We observed the region described above alternately through the full *K*-band filter and an He I 2.09-μm narrow-band ($R=150$) filter. In addition we took sky data through both filters near the flux-calibrator source 9 Sgr. During the 1996 April and June observing runs we took two data sets each with the dispersion in north–south and east–west directions. For each data set the total number of recorded dispersed speckle images was between 1500 and 2000. The short-exposure seeing was of the order of 0.6 arcsec for the 1996 April run and between 0.6 and 1.0 arcsec for the 1996 June run. The raw images were sky-subtracted, a flat-field was applied and dead pixels were corrected for by interpolation. The spectrally dispersed data can be flat-fielded since the relative spectral response of individual pixels at the chosen spectral resolution is the same to within ≤ 1 per cent. This was checked independently by comparing spectra across the final objective prism images and by comparing

flat-field data taken through 2.058-μm He I, 2.165-μm Brγ, and 2.29-μm CO narrow-band filters with a spectral resolution of $R=150$ in 1994 (Eckart et al. 1995).

2.3.1 *Speckle spectroscopy image formation*

Speckle spectroscopic interferograms $IS(x,y)$ can be thought of as the usual short-exposure image $I(x,y)$ of a seeing cloud – i.e. the image of the object $O(x,y)$ convolved with the atmospheric point spread function $PSF(x,y)$ – convolved with a product of the source K-band spectrum $K(x)$ and the combined K-band atmospheric and instrumental spectral response function $SP\{K\}(x)$:

$$IS(x,y)=I(x,y)*[K(x)SP\{K\}(x)]$$
$$=[O(x,y)*PSF(x,y)]*[K(x)SP\{K\}(x)]. \quad (1)$$

In speckle image reconstructions for point-like objects (stars) the product $O(x,x)*PSF(x,y)$ can be represented by an Airy pattern, the image of the star at the K-band diffraction limit of the NTT telescope which is of the order of 0.15 arcsec. For our 1-arcsec long K-band spectrum we can therefore expect at the diffraction limit a maximum spectral resolving power of about $R=35$. In order to extract the spectral information we have to obtain an independent measure of the atmospheric point spread function. This is achieved by interleaving the observations described with observations of the same field (containing the structural calibrator source IRS7) through the combination of the objective prism and the $R=150$ He I 2.09-μm narrow-band filter. With $SP\{\mathrm{NB}\}(x)$ we denote the corresponding combined atmospheric and instrumental response function. The spectral resolution of the narrow-band filter is higher than what we can obtain with our speckle spectroscopic observations described above. Therefore the narrow-band filter spectral response function $SP\{\mathrm{NB}\}(x)$, as well as its product with the source spectrum $K(x)$, can be approximated by a delta function $\delta(x-x_{\mathrm{NB}})$, where x_{NB} corresponds to the centre wavelength of the NB filter. Individual reference speckle interferograms $IR(x,y)$ of the IRS7 reference source $REF(x,y)$ can then be written as

$$IR(x,y)=I(x,y)*[K(x)SP\{\mathrm{NB}\}(x)]=$$
$$=[REF(x,y)*PSF(x,y)]*[K(x)SP\{\mathrm{NB}\}(x)], \quad (2)$$

or

$$IR(x,y)=[REF(x,y)*PSF(x,y)]*\delta(x-x_{\mathrm{NB}})$$
$$=REF(x,y)*PSF(x_{\mathrm{NB}},y). \quad (3)$$

This way we can record images of the structural calibrator through the objective prism at the same telescope focus. Alternated observations through the full K-band filter and through the narrow-band filter allow us to sample the statistical variations of the atmospheric point spread function and to seeing-correct the dispersed speckle data.

2.3.2 *Using the simple-shift-and-add algorithm for speckle spectroscopy*

For both spectral resolutions we carried out the speckle-image data reduction with the simple-shift-and-add algorithm (SAA: Eckart et al. 1994; Christou 1991). For the narrow-band filter the images are identical to ordinary non-dispersed speckle interferograms and the application of the SSA algorithm is straightforward. From the resulting SSA images we then extract the structural calibrator image of IRS7. Owing to the combined atmospheric and instrumental transmission function, and most of all the high reddening of the Galactic Centre sources, the raw spectra of the stars are sharply peaked in the red. This allows us to apply the SSA algorithm for the spectrally dispersed K-band images as well.

We tried a variety of methods to determine the SSA shift vectors. The highest spatial and spectral resolution SSA images were obtained using a matched-filter approach. This ws done by searching through individual short exposures and extracting an image of a single, bright, dispersed IRS7 speckle that is sufficiently isolated from the overall seeing cloud and using it as a matched filter. We calculated the cross-correlation between this spectrum and all the individual images of the full speckle interferograms. The peak in the cross-correlated image of IRS7 then denotes the corresponding location of the brightest dispersed speckle in each image. The difference between this location and the long-exposure centroid of the IRS7 images was used as a shift vector in the SSA process.

The resulting broad-band spectrally dispersed SSA images were then deconvolved with the point spread function obtained from the narrow-band SSA images on IRS7 using the Lucy–Richardson algorithm (Lucy 1974). After 2000 iterations the deconvolution was stopped because a resolution close to the diffraction limit of the NTT was reached orthogonal to the dispersion direction. The resulting deconvolved images consist of objective-prism spectra of the stars in the central stellar cluster close to the diffraction limit of the NTT (Fig. 3a). The length of the spectra corresponds very well to the predicted dispersion of 1 arcsec for the whole K band. For comparison we also show the non-dispersed image convolved with the measured raw spectrum of IRS16NW (Fig. 3d). This frame shows the same structures as the deconvolved spectrally dispersed SSA data. The comparison indicates that the deconvolved SSA image (Fig. 3a) contains all of the expected structures.

2.3.3 *Extraction and calibration of spectra*

Knowing the exact relative positions of the stars we can now extract their individual spectra. The relative spectral calibration is carried out using the almost featureless star IRS29N (Krabbe et al. 1995; Genzel et al. 1996). The quotient between the extracted spectrum of any star with the raw IRS29N spectrum can then be multiplied with the calibrated spectrum of IRS29N, as published in Krabbe et al. (1995), convolved to the spectral resolution of our speckle spectroscopy data. The absolute wavelength calibration was obtained using the sharp intensity cut-offs at the K-band filter edges. Owing to the three-fold oversampling of the diffraction limit in the SHARP1 camera the accuracy of the wavelength calibration is about three times better than the spectral resolution of the data. In Fig. 4 we show the spectra of another featureless source, IRS3, a typical late-type star, IRS13W, and two typical He I emission-line stars, IRS16SW and IRS16NW. These spectra demonstrate that the overall spectral shape as well as the prominent CO

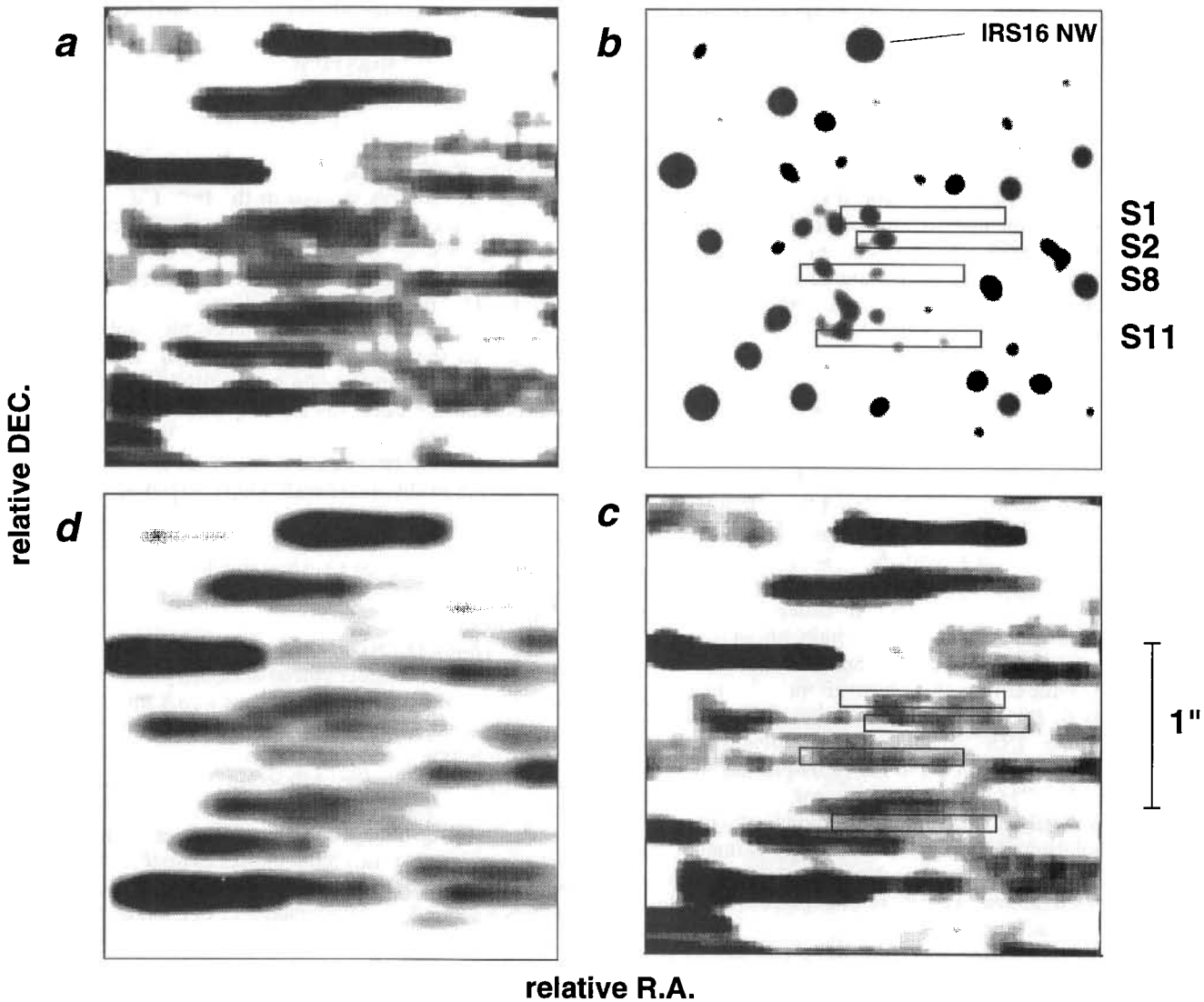

Figure 3. Speckle spectroscopy of the central 3.5×3.5 arcsec^2. (a) Deconvolved objective prism image spectrally dispersed in the east–west direction. (b) Non-dispersed image with boxes indicating the areas from which the spectra of the sources S1, S2, S8 and S11 have been extracted. (c) Dispersed deconvolved SSA image corrected for the contaminating flux contribution of S3, S4 and the weak sources 0.2 to 0.3 arcsec west and east of S8 to S11. The areas over which the spectra of sources S1, S2, S8 and S11 are extracted are indicated by boxes. (d) Non-dispersed image convolved with the measured raw spectrum of IRS16NW. This frame shows the same structures as the deconvolved spectrally dispersed SSA data. The comparison indicates that the deconvolved SSA image (a) contains all the expected structures.

bandhead absorption feature can be clearly discerned in the low-resolution spectra. The narrower He I emission line, however, is too much diluted at $R \sim 35$ for reliable detection. These spectral features were used to verify the wavelength calibration.

2.3.4 *Extracting spectra in the Sgr A* cluster*

In Fig. 3(a) we show the central 3×3 arcsec^2 of the deconvolved image spectrally dispersed in the east–west direction. A comparison with the non-dispersed image in Fig. 1(b) demonstrates that there is significant flux at the position of the central Sgr A* sources. In these images the sources S1, S2, S8 and S11 are the least contaminated by strong sources in the IRS16 complex. In order to obtain reliable spectra of some of the sources we used the best east–west dispersed SSA results from 1996 April and June and calculated the mean spectra and error estimates.

In Fig. 3(b) we show, in a non-dispersed speckle-image reconstruction, the area over which we extracted the spectra of the selected central Sgr A* sources. The spectra were either extracted directly from the SSA frames (step A) or from frames in which the contaminating flux density of neighbouring sources was removed (step B). In order to do so we first extracted the positions and relative flux densities of the contaminating sources from a high-resolution speckle-image reconstruction. A first-order correction for the contamination was then achieved by subtracting a spectrally dispersed SSA image of a calibrator source that is featureless at our resolution with the appropriate flux density scaling at these positions. In Fig. 3(c) we show a dispersed, deconvolved SSA image, corrected for the con-

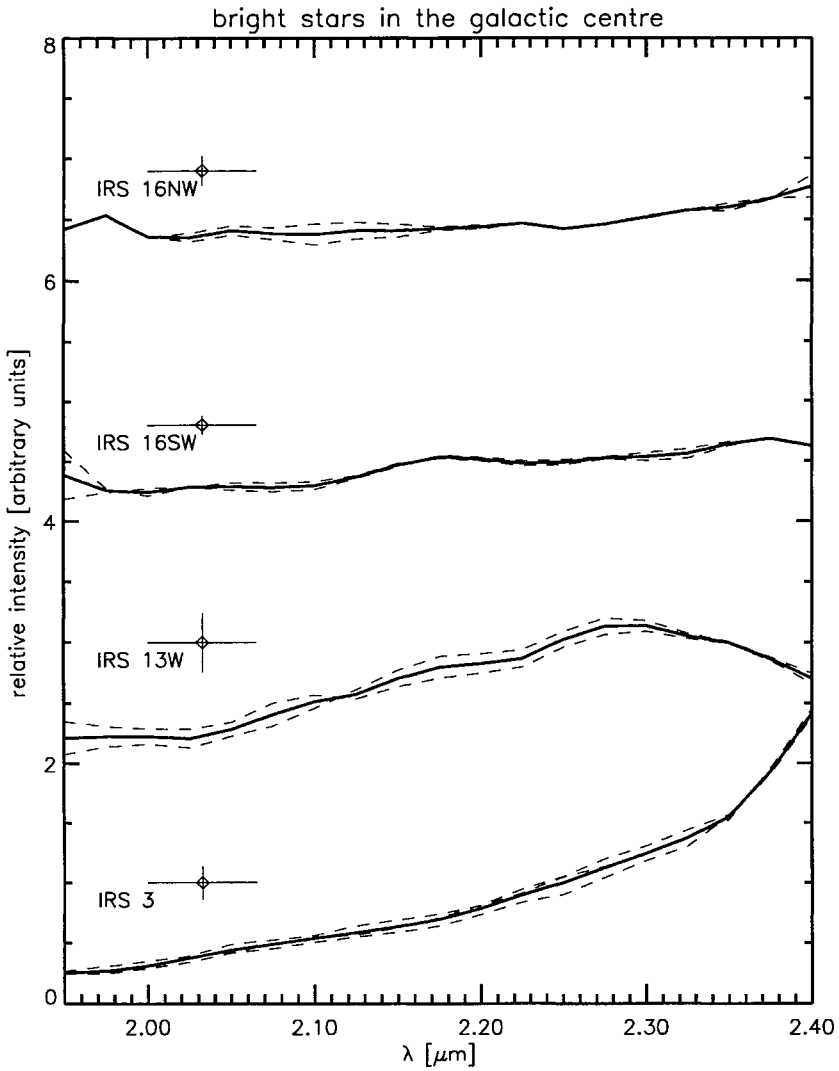

Figure 4. Extracted and calibrated speckle spectra of the featureless source IRS3, a typical late-type star (IRS13W) and the He I stars IRS16SW and IRS16NW. The thick black line represents the mean of the individual dashed spectra that resulted from our best SSA images from 1996 April and June. The spectral resolution of $\lambda/\delta\lambda = 35$ as well as the 1σ error is indicated by the cross. The spectra compare well with the $\lambda/\delta\lambda = 1000$ spectra of these sources presented by Krabbe et al. (1995).

taminating flux contribution of S3, S4 and the weak sources 0.2 to 0.3 arcsec west and east of S8 to S11.

In a first step the spectrum of the featureless calibrator was extracted directly at its position and in the corresponding frame (step C). In a second approach (step D) we extracted the calibrator spectrum from a calibrator image at the position of the corresponding program source to which the calibration had to be applied. The calibrator image was obtained by convolving a non-dispersed SSA image of the same region with the IRS29N calibrator spectrum. This image was then deconvolved with the corresponding point spread function taken from the non-dispersed SSA image using the same number of iterations as for the measured dispersed frames. In the same way as described above, the deconvolved frame was then corrected for the contaminating flux density of neighbouring sources in the vicinity of the central Sgr A* cluster. The calibrator spectrum was then extracted from exactly the same position as the spectrum of the program sources. This method allows us to correct for all possible residual local artefacts due to the imperfections in the correction of the contaminating sources.

We divided all combinations of program spectra (extracted via methods A and B) and calibrator spectra (extracted via methods C and D) and multiplied the quotients with the known spectrum of the calibrator source as described above. All combinations resulted in very comparable calibrated spectra. In order to test the reliability of our procedure we created an object test image from one of the spectrally dispersed SSA images. In this frame we modified the spectra of S1 and S8, by adding a point spread function convolved version of an artificial spectrum that has a CO absorption bandhead with a mean depth of about half the continuum and a bright line at the position of the He I emission line, with variable line-to-continuum ratio. The convolved artificial spectra were, of course, scaled to the appropriate intensity of the sources in the SSA frame. After deconvolution we calculated spectra at the positions of S1 and S8 using a combination of steps B and D. This combina-

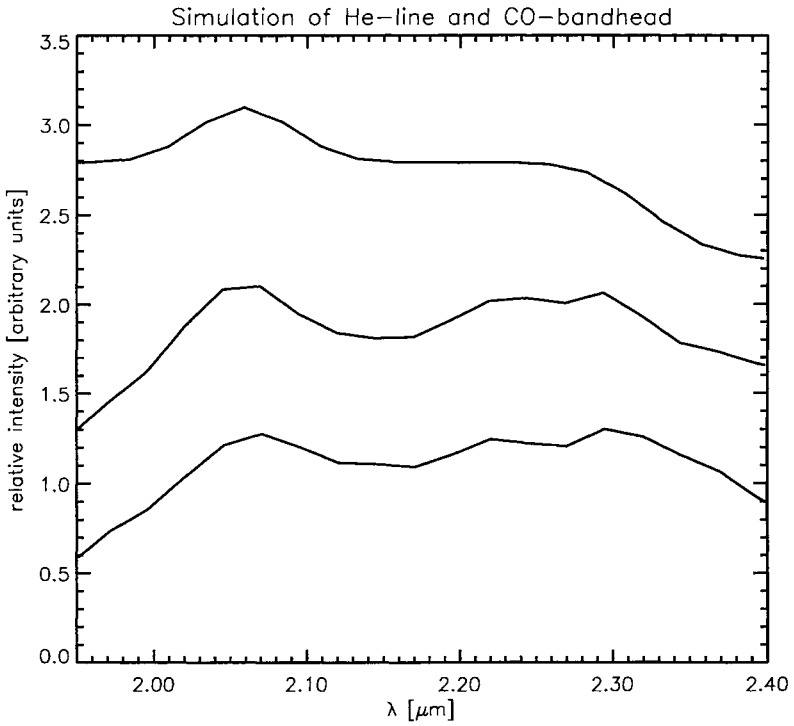

Figure 5. Deconvolution test carried out on the sources in the Sgr A* cluster. Top: differential synthetic object input spectrum convolved with a Gaussian of 3-pixel width (the effective spatial and spectral resolution) showing a CO bandhead absorption and an emission line at the wavelength of the He I line. Middle: expected output spectrum calculated by adding the above differential input spectrum to the measured spectrum of S8. Bottom: resulting measured simulated spectrum. The synthetic input spectrum had been convolved with the spatial PSF and added to the April SSA frame at the position of source S8. The data analysis was then carried out as for all other sources and as described in the text. This result indicates that all line features can be recovered successfully, if present.

tion represents the best calibration and correction of possible residual contamination of neighbouring sources. Fig. 5 shows the differential and effective synthetic object input spectrum and a calibrated output spectrum extracted at the position of S8. All of the input line features are present, thus demonstrating the validity of the calibration approach. This test shows that we can detect CO bandhead absorption or strong line emission if they are present in the Sgr A* sources.

3 RESULTS

3.1 Deep maps of the Sgr A* cluster and possible detection of an Sgr A* infrared counterpart

Fig. 1 shows grey-scale representations of the best and deepest *K*-band maps (1996 April and June) of the central 3-arcsec diameter region that we have so far been able to construct. They were assembled from $\sim 3 \times 10^4$ frames of 0.5-s integration each (50-mas pixels) taken in 0.4- to 0.7-arcsec seeing. In the case of the 1996 June map we also added in a map taken with 25-mas pixels that was obtained by mounting an appropriate magnifying lens in front of the camera. Because of the excellent quality and high signal-to-noise ratio of these data sets (3σ limiting *K*-band magnitude ~ 17) we were able to confidently achieve a factor of 2 super-resolution of the images, resulting in the ~ 0.07 arcsec FWHM final maps in Fig. 1. These maps confirm that the Sgr A* (infrared) complex consists of individual stars. Within a projected distance from Sgr A* of $p \sim 0.5$ arcsec, Fig. 1 shows ~ 20 stars between $m(K) \sim 13$ and 16, with the following magnitude distribution. There are three stars with $m(K) \leq 14$, nine stars with $m(K) \leq 15$ and 20 stars with $m(K) \leq 16$. This distribution is consistent with an evolving cluster of age > 1 Gyr, constant star formation and a 'Salpeter' initial mass function [$\mathrm{d}N(M) \sim \mathrm{M}^{-2.4}\ \mathrm{d}M$]. While the number of stars is still too small to constrain, in any meaningful way, the shape of the mass function, our data suggest that the observed stars are the 'tip of the iceberg' of fainter and lower mass stars that are likely present below our current detection limit. Note that all of the stars we are currently sampling in the Sgr A* cluster with the SHARP1 maps have masses in excess of 10 $\mathrm{M}_\odot$ (unless they are late-type stars, which we will exclude below). This implies that these stars have had to form less than a few times 10^7 yr ago. This may be surprising at first if one pictures the Galactic Centre as an 'old' stellar cluster. However, the observational evidence for fairly recent ($3\text{–}9 \times 10^6$ yr ago) massive star formation in the central pc is now very strong (Allen, Hyland & Hillier 1990; Krabbe et al. 1991, 1995).

The nomenclature of the Sgr A* cluster sources marked in Fig. 1 is as in EG. The comparison of the two epochs shows the excellent overall agreement of the data sets. A certain tendency for fainter stars to show larger discrepancy in flux between the two epochs (this is also true for the earlier epochs in Fig. 2) may be largely ascribed to the increasing uncertainty of photometry at the faintest levels when analysing such a crowded region. We refer to Appen-

dix A for detailed comments on individual sources. In addition, there are also a few significant differences that we interpret as source variability. In particular there appears to be an $m(K) \sim 15$ source (S12) between S1, S2 and S3 in the 1996 June epoch that was not detected in 1996 April (or at an earlier epoch: Fig. 2). In April any source at that position would have been fainter than $m(K) \sim 16.3$. The location of S12 is coincident with the compact radio source Sgr A*, to within the ± 30-mas uncertainties of the radio–infrared reference frames (Menten et al. 1997). S12 may thus be the best candidate yet for an infrared counterpart to the compact radio source Sgr A*. S12 appears to be time variable.

3.2 Spectra in the central Sgr A* cluster

Since the field around Sgr A* is very crowded (Fig. 1) most of the spectra are contaminated by other nearby stars. The central Sgr A* cluster, however, is located west of the IRS16 complex in a void of bright stars. The separation to any bright star is larger than 1 arcsec, and the contaminating effects of neighbouring sources are comparatively small. About half of the Sgr A* cluster sources are distributed in north–south direction. We have exploited this lucky coincidence to extract low-resolution spectra of individual stars in this region. We have described in Section 2.3 the techniques employed for reducing the data and obtaining spectra from speckle data at near-diffraction-limited spatial resolution. In Fig. 6 we show the spectra of the sources S1, S2, S8 and S11 obtained with a combination of the two extraction techniques discussed above. The resulting spectra are fairly flat and increase slowly in flux towards longer wavelength. *CO bandhead absorption is absent so S1, S2, S8 and S11 cannot be late-type giant stars.* While somewhat redder than the most prominent He I emission-line stars in the IRS16 complex (Fig. 4), their spectral characteristics are consistent with early-type stars located in the central cluster [i.e. $A(K) \sim 3$]. There is also no indication for very strong line-emission (or absorption) at the wavelength of the He I and/or Brγ emission lines. This is not surprising, however, as the narrow He I/Brγ emission lines cannot be seen even in the classical He I emission-line stars at the low spectral resolution we have used (Fig. 4). These results are fully consistent

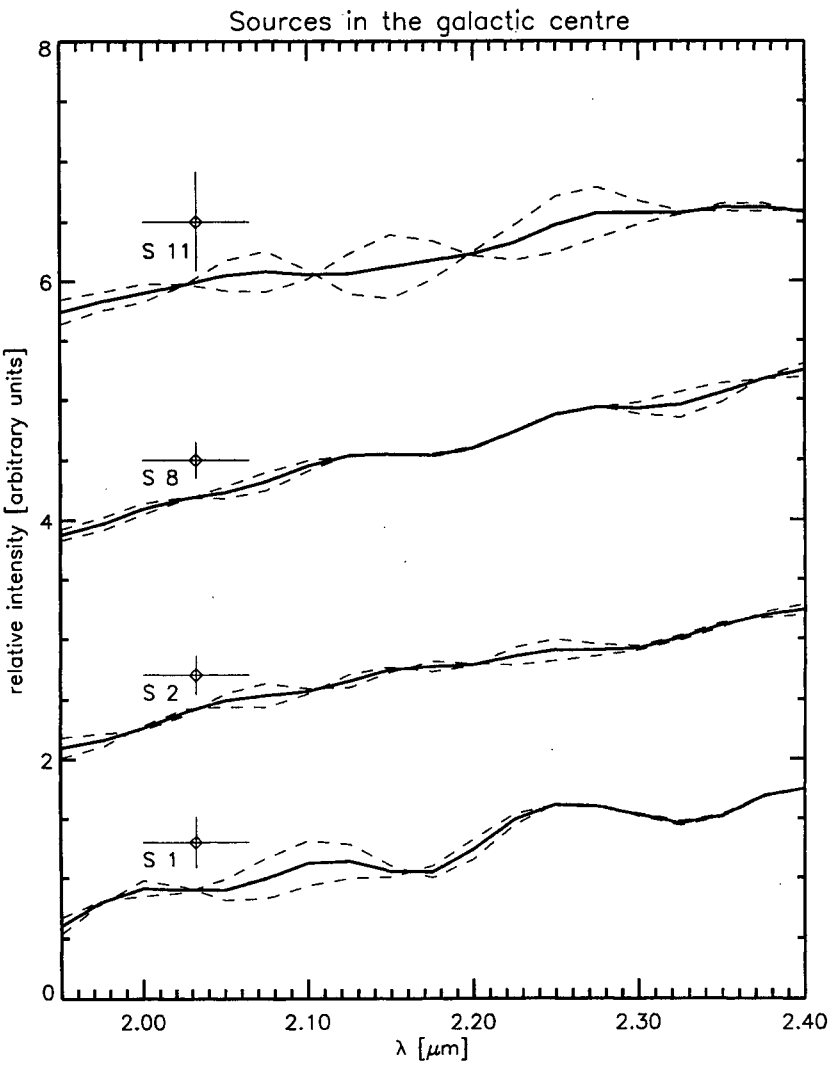

Figure 6. Extracted and calibrated speckle spectra of the sources S1, S2, S8 and S11 obtained from our speckle spectroscopy data as described in the text. The thick black lines represent the mean of the two best data sets from 1996 April and June.

with the broad-band *JHK* colours and narrow-band filter data presented in Eckart et al. (1995). We conclude that *the $m(K) \sim 14.5$ sources in the central Sgr A* cluster are most likely moderately luminous ($L \sim 5000$ to 10 000 $L_\odot$) early-type stars.* If they are on the main sequence they would have to be O9–B0.5 stars with masses of 15 to 20 $M_\odot$.

3.3 Constraints on the mass distribution from stellar motions

3.3.1 Proper motions

EG and Genzel et al. (1996) have discussed the presently available stellar radial and proper motions in the central parsec of the Galactic Centre. They find strong evidence for the presence of a compact (size ≤ 0.1 pc), dark ($M/L \geq 100$) mass concentration ($M = 2.45(\pm 0.4) \times 10^6$ $M_\odot$) centred on or near the compact radio source Sgr A* (e.g. Backer 1994, 1996). From a four-epoch analysis between 1994 and 1996 EG found that several of the components appear to move in excess of 1000 km s^{-1} (for a Sun–Galactic Centre distance of 8.0 kpc). The most significant of these are S1 ($v_{sky} = 1660 \pm 400$ km s^{-1}) and S4 ($v_{sky} = 1040 \pm 450$ km s^{-1}) $\{v_{sky} = [(v_x)^2 + (v_y)^2]^{1/2}\}$. With the relative astrometry of Menten et al. (1997) both of these components are within 0.2 arcsec of the compact radio source Sgr A*.

The following simple statistical consideration shows that the overwhelming fraction of stars within the ~ 1-arcsec diameter Sgr A* cluster are very likely close to the radio source and not just projected foreground or background objects. From counting all reliably detected sources with $m(K) \leq 16.5$ in Fig. 1 the source density is 20 $[\pm 4 = (20)^{1/2}]$ stars per arcsec^2. In the adjacent region ~ 1 arcsec west of Sgr A* (where crowding, number of bright sources, etc., is very similar to the Sgr A* cluster) the source density is 9 (± 3) source per arcsec^2. This indicates that the Sgr A* cluster likely does represent an intrinsic, local overdensity of (faint) stars. The statistical significance of this overdensity is presently at the 3σ level and is limited by the numbers of objects that can be detected. How large is the possible contamination by foreground and background stars? The surface density of stars in the Sgr A* cluster with $m(K) \leq 15$ is 14 ± 4 stars per arcsec^2. For comparison the stellar surface density outside the central arcmin (i.e. outside the prominent nuclear concentration: see Gatley et al. 1989) is ≤ 0.1 stars per arcsec^2 and decreasing approximately as p^{-1} beyond $p = 4$ arcsec (Eckart et al. 1993, and in preparation). From the ratio of areas one would thus expect to find no more than one such distant star within a radius of 3 arcsec of Sgr A*. Stars significantly outside the Galactic Centre area also would have a different infrared colour, as their extinction would be different from stars in the central arcmin. In fact one such star (CCD 2: Storey 1982; source A: Biretta, Lo & Young 1982; NIR 1: Ricker et al. 1982) with unusually blue colour is located about 1 arcsec north-north-east of Sgr A* (Rosa et al. 1992). Next, consider a smaller volume of radius ~ 10 arcsec (0.4 pc) relative to Sgr A*, close to the core radius of the faint late-type stars (Genzel et al. 1996). There should be about one star in this volume whose projected position lies within the Sgr A* cluster (radius ~ 0.5 arcsec). Hence it is statistically very likely that an overwhelming fraction (> 80 per cent) of the Sgr A* cluster members are indeed located in a volume of radius no more than 1 or 2 arcsec). We conclude that the Sgr A* cluster thus is likely a local concentration (a cusp) of stars in the immediate vicinity of the radio source.

We have described above our reanalysis of the proper motion data including a good data set from the 1992.65 epoch, thus approximately doubling the time baseline as compared with the data used by EG. We have also added to our proper motion analysis 18 stars between $p = 0.9$ and 2.9 arcsec, mostly west and south-west of Sgr A*, that we had not included in our previous analysis (W1 to W18 in Table 1). With respect to brightness and crowding this region is quite comparable to the Sgr A* cluster region. The results of our reanalysis are given as 0.15 arcsec resolution astrometric maps of the *K*-band emission for the different epochs (Fig. 2), as position–time plots (Fig. 7) and as a list of RA and Dec. velocities in Table 1. One important check of these images is a comparison to the first available high-resolution maps obtained recently by other groups. Klein et al. (1996) have presented a 1995.5 epoch, 0.05 arcsec resolution *K*-band speckle map obtained with the Keck telescope. It compares very well with our 1995 epoch image (Fig. 2), including the positions of the key high-velocity stars. Rigaut et al. (in preparation) have obtained a 1996.5 epoch, 0.15-arcsec *K*-band adaptive optics image taken with the 3.6-m Canada–France–Hawaii telescope. Again their image is in excellent agreement with our 1996 June data sets in Figs 1 and 2. *We thus conclude that the images of Figs 1 and*

Table 1. Proper motions in the Sgr A* cluster and the region ~ 1 arcsec west of it; the epoch is 1994.27.

Source	m(K) (1996.4)	$\Delta\alpha$ (arcsec)	$\Delta\delta$	v(EW) (km/s)	σ(EW)	v(NS) (km/s)	σ(NS)
S1	14.5	-0.09	+0.07	990	350	-1200	350
S2	14.0	+0.01	+0.17	40	350	-690	350
S3	15.5	+0.11	-0.06	-1200	400	-50	400
S4	14.0	+0.18	+0.06	1300	350	220	350
S5	16.0	+0.29	+0.15	730	500	330	500
S6	14.5	+0.43	+0.07	310	500	160	500
S7	15.5	+0.61	-0.08	130	500	-600	550
S8	14.5	+0.28	-0.15	870	350	-650	400
S9	15.5	+0.20	-0.28	-110	800	-1790	800
S10	14.0	+0.14	-0.44	-380	600	-600	600
S11	14.5	+0.11	-0.53	600	600	-750	600
W1(29S1)	9.9	-1.90	+0.90	150	200	70	200
W2(29S2)	10.7	-1.98	+0.80	70	200	150	200
W3	14.0	-2.53	+0.40	-350	250	-170	250
W4	13.5	-1.29	+0.52	20	150	-220	150
W5	13.5	-0.84	+0.34	-180	150	-420	150
W6	13.5	-0.51	+0.34	350	200	100	150
W7	12.5	-1.68	+0.11	100	200	-230	200
W8	13.5	-1.16	-0.09	130	200	380	200
W9	13.0	-0.73	-0.28	270	200	60	200
W10	12.5	-1.32	-0.26	130	150	-390	150
W11	13.5	-0.66	-0.85	670	200	-280	200
W12	13.5	-1.04	-0.86	-520	200	-460	200
W13	13.0	-0.86	-0.99	300	200	-280	200
W14	11.5	-1.68	-0.54	350	150	-150	150
W15	14.5	-1.83	-1.19	-250	250	-10	250
W16	13.0	-2.27	-0.94	390	250	300	200
W17	13.0	-2.48	-0.84	130	300	10	150
W18	13.0	-2.72	-0.34	150	150	180	150

The source positions are given with respect to the radio position of Sgr A*. The 1σ error on this position is approximately ± 30 mas.

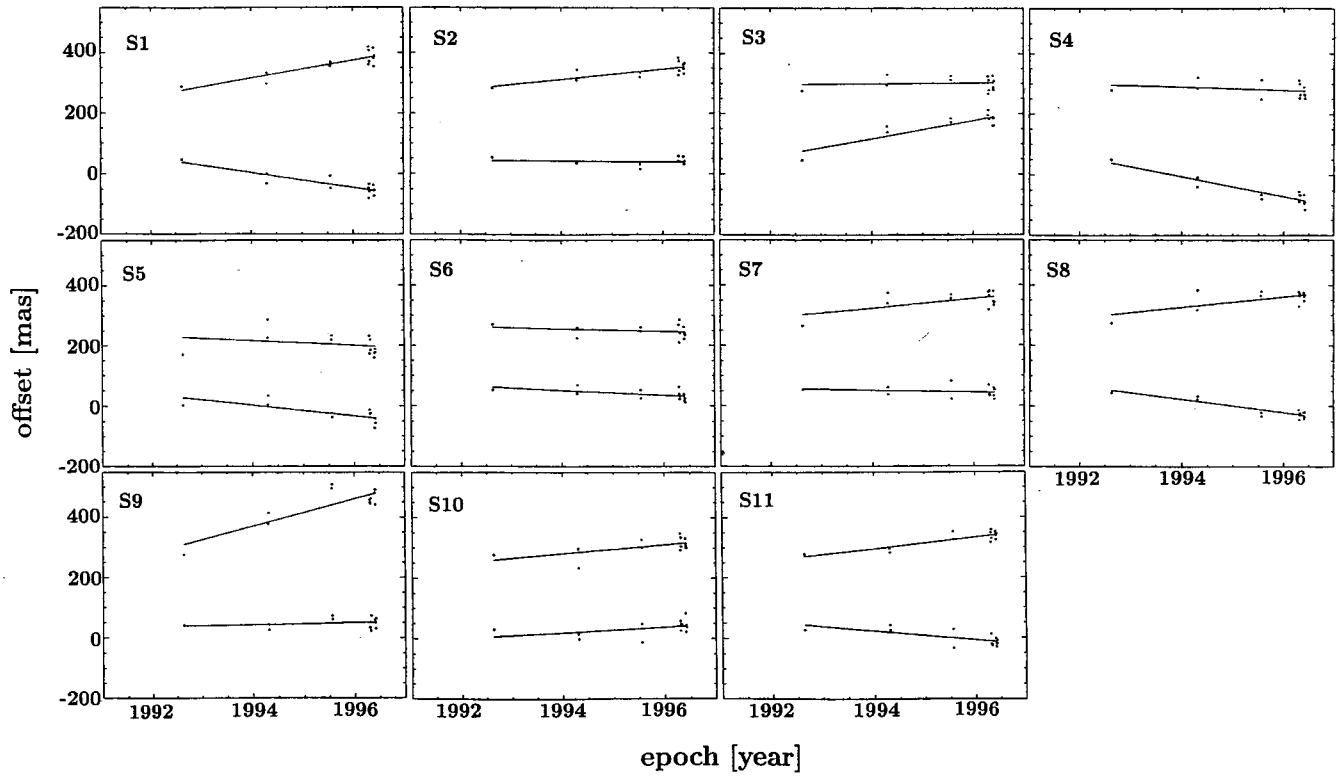

Figure 7. Position–time plots for sources S1–S11 in Table 1. The panels show the x-($\sim$RA) and y-($\sim$Dec.) positions as a function of time, along with the best-fitting proper motions (straight lines). Offsets are relative to the positions determined at the base epoch. Positions of the different independent data sets in each epoch are shown as black dots. For display purposes the graph showing the Dec. motion has been offset by $+300$ mas.

2 are robust and that the source structure does indeed change with time. The most probable interpretation of these changes is that the stars in the Sgr A* cluster are moving rapidly (EG).

The resulting proper motions confirm the results of EG. In particular, the 1992 positions of the high-velocity stars S1, S4 and S8 are fully consistent with the backward extrapolation of the EG data. The individual proper motions for these stars are now detected at 4.4, 3.3 and 2.9 times our measurement uncertainty. S3 also appears to have an $\sim$1000 km s^{-1} motion (detected with $\sim 3\sigma$ significance), although this source becomes more difficult to track with certainty in 1996. A very important fact is that the positions change monotonically over four years (five epochs). This makes it very likely that we are, indeed, seeing orbital stellar motions and not a 'Christmas tree' effect connected to variability in a crowded environment. Furthermore, the evidence for high-velocity stellar motions no longer rests on a single, special case. Our reanalysis also shows that the region S9/S10/S11 (and to a lesser extent S5/S6) is dangerously crowded, so that we have given these stars lower weight in the following analysis. None of the velocities for the 18 new stars west of the Sgr A* complex ($0.9 \leq p \leq 2.9$ arcsec: Table 1) has yet been detected with high significance ($\geq 4\sigma$). Three or four stars have motions $\geq 3\sigma$. However, as a group these stars do support the evidence for a rapid decrease of average velocities away from Sgr A*. They also significantly improve the statistics of motions between 1 and 3 arcsec.

3.3.2 *Mass models*

In Table 2 we list the resulting intrinsic velocity dispersions (corrected for measurement bias) and enclosed masses as a function of radius from the dynamic centre assumed to be at Sgr A*. For stars outside the Sgr A* cluster we have determined these mass estimates from a Jeans equation analysis as described in EG and Genzel et al. (1996). We used the $K \leq 14$ surface density counts of Eckart et al. (1995) to obtain the stellar number density as a function of distance from Sgr A*. In the case of the dozen stars within the Sgr A* cluster itself ($p \leq 0.7$ arcsec: $\sigma = 560 \pm 90$ km s^{-1}), a separate determination of the enclosed mass via the virial and Bahcall–Tremaine (1981) projected mass estimators is more appropriate than including this point in the Jeans analysis together with the data at $p \geq 1$ arcsec. The reason is that – as mentioned above – the stars near Sgr A* likely form a distinct, local concentration of much smaller core radius than that of the other stars. In addition, Table 2 also lists velocity dispersions and mass estimates obtained via Jeans analysis from the radial velocities of stars (Genzel et al. 1996, using additional data from Rieke & Rieke 1988, McGinn et al. 1989, Sellgren et al. 1990, Lindqvist, Habing & Winnberg 1992, Krabbe et al. 1995 and Haller et al. 1996). We also include two mass points at $R \geq 1.5$ pc determined from the gas velocities in the rotating, circumnuclear disc (Guesten et al. 1987). For the stellar dynamics the 1σ errors of velocity dispersions and masses (after accounting properly for measurement bias) are mainly determined by

Table 2. Derived velocity dispersions and enclosed masses.

p (arcsec)	number of proper motions	σ (km/s)
0.27" (interval: 0-0.7")	24	560±90
1.15" (0.7-1.5")	22	275±42
2.0" (1.5-2.5")	44	171±19
3.4" (2.5-6")	36	132±16

R (pc)	M(R) (x10^6 M$_\odot$)	method	reference
0.016	2.65±0.76	prop.mot.,projected mass estimators	this paper
0.07	2.8±1.1	prop.mot., Jeans	"
0.094	2.5±1.5	rad.mot., Jeans	Genzel et al.96
0.12	2.54±0.6	prop.mot., Jeans	this paper
0.14	2.8±1.5	rad.mot., Jeans	Genzel et al.96
0.19	2.5±0.75	"	"
0.21	2.51±0.4	prop.mot., Jeans	this paper
0.24	2.9±0.87	rad.mot., Jeans	Genzel et al.96
0.28	3.0±0.84	"	"
0.33	3.15±0.75	"	"
0.38	3.3±0.56	"	"
0.56	3.3±0.56	"	"
0.75	3.6±0.36	"	"
0.94	3.95±0.38	"	"
1.5	4.5±0.95	rotating gas disk	Guesten et al.87
1.9	5.7±0.97	rad.mot., Jeans	Genzel et al.96
3.8	11.2±1.9	"	"
4	11±2.8	rotating gas disk	Guesten et al.87
11.3	30±4.8	rad.mot., Jeans	Genzel et al.96

the $N^{-1/2}$ statistical errors due to the number of motions measured (two for each star with a proper motion). Proper motion measurement errors obviously have a significant, but not dominant, impact on the derived velocity dispersions and masses in the innermost region. To test the influence of our error estimates on the results we artificially varied the 1σ velocity errors in the Sgr A* cluster from 300 to 500 km s^{-1}. This changes the velocity dispersion of the 12 stars with $p \leq 0.7$ arcsec from 590 ± 95 to 510 ± 80 km s^{-1}. Different choices of measurement errors thus introduce an error in the resulting velocity dispersion of approximately ± 40 km s^{-1} (as compared with the statistical error of ± 90 km s^{-1}). Further out the impact of measurement errors on the derived velocity dispersion is lower. Different binning in radius naturally also has a significant impact on the derived quantities, as the numbers of stars in each bin are still relatively small (12 to 22 stars). This effect is also smaller than the statistical errors and averages out in the overall mass model.

As discussed in our earlier papers the data are fitted extremely well by the combination of a point-mass plus an extended cluster of stars with an isothermal density distribution and a core radius of 0.25–0.5 pc. This stellar cluster fits the *K*-band light distribution of faint, late-type stars with a mass to *K*-band luminosity ratio of ~ 2 M$_\odot$/L$_\odot$ (Genzel et al. 1996). This is shown in Fig. 8, which is a plot of all mass estimates in the central 10 pc, along with model fits for the visible stellar cluster (thick dashed curve) and point-mass plus visible cluster (thin continuous curve). A χ^2-analysis of

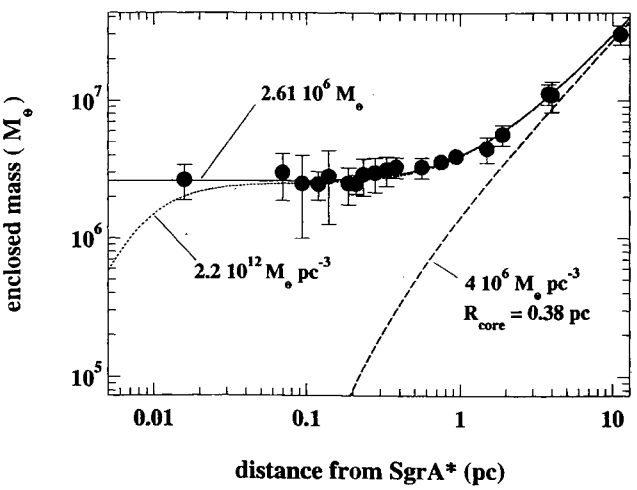

Figure 8. Mass modelling of the stellar proper and radial motions, with the addition of two points from gas kinematics at $R = 1.5$ and 4 pc. Shown as filled circles with 1σ error bars are the various mass estimates listed in Table 2 and discussed in the text, assuming a Sun–Galactic Centre distance of 8 kpc. The thick dashed curve represents the mass model for the (visible) stellar cluster [M/L (2 μm) = 2, $R_{core} = 0.38$ pc, $\rho(R=0) = 4 \times 10^6$ M$_\odot$ pc^{-3}: Genzel et al. 1996]. The thin continuous curve is the sum of this stellar cluster, plus a point mass of 2.61×10^6 M$_\odot$. The thin dotted curve is the sum of the visible stellar cluster, plus an $\alpha = 5$ Plummer model of a dark cluster of central density 2.2×10^6 M$_\odot$ pc^{-3} and R$_\odot$ = 0.0065 pc (equation 4). It provides a χ^2 fit 1σ worse than the best fit with central density $\geq 7.5 \times 10^{13}$ M$_\odot$ pc^{-3}.

19 radial and proper motion mass estimates (including the new results presented here) from Table 2 now gives a best-fitting point-mass of 2.61×10^6 $M_\odot$ with a 1σ statistical uncertainty of $\pm 0.5 \times 10^6$ $M_\odot$ (8, as compared with $2.45 \pm 0.25 \times 10^6$ $M_\odot$ in EG). Adding to this the systematic uncertainty we estimate a total uncertainty of $\pm 0.35 \times 10^6$ $M_\odot$. The proper motion data strongly suggest that the location of the dark mass is within 0.2 arcsec (10^{16} cm) of Sgr A*.

3.3.3 *Minimum density of central dark mass*

Next we have explored the minimum density of a dark cluster of non-zero core radius that fits the data (in combination with the visible stellar cluster). One estimate can be obtained from the innermost high-velocity stars, assuming that they are just bound, that their radial velocities are not significant and that their true radius R is close to the projection p on the sky relative to Sgr A*. In this case a lower limit to the mass enclosed within p is $M_{\rm min}(<p) \geq v_{\rm sky}^2 p/(2G)$. For S1 $M_{\rm min}$ is $2.4 \pm 1 \times 10^6$ $M_\odot$, for S3 $M_{\rm min}$ is $5.8 \pm 3.9 \times 10^5$, for S4 $M_{\rm min}$ is $5.6 \pm 4.8 \times 10^5$ $M_\odot$ and for S8 $M_{\rm min}$ is $1.6 \pm 1.1 \times 10^6$ $M_\odot$. The corresponding density of the central mass is $\rho_{\rm min} = 3v_{\rm sky}^2/(8\pi G p^2)$; it is 1.4×10^{12} $M_\odot$ pc^{-3} for both S1 and S4, 3.2×10^{12} $M_\odot$ pc^{-3} for S3 and 2×10^{11} $M_\odot$ pc^{-3} for S8.

For a second estimate we assume that the density distribution of the dark cluster is described by a Plummer model of index $\alpha = 5$. Such a 'hard core' model is clearly required by the very flat distribution of dark mass between 0.01 and 0.4 pc. A Plummer model has a stellar volume density distribution of

$$\rho(R) = \rho_0 [1 + (R/R_0)^2]^{-\alpha/2}. \quad (4)$$

We find that the best-fitting dark cluster must have a density of $\rho_0 \geq 7 \times 10^{13}$ $M_\odot$ pc^{-3} ($R_0 = 3$ mpc) but that a dark cluster of density $\sim 2.2 \times 10^{12}$ $M_\odot$ pc^{-3} ($R_0 = 6.5$ mpc) has a significance only 1σ lower than the best value. This just acceptable dark cluster model is shown as a thin dotted curve in Fig. 8. A density of $\sim 2.2 \times 10^6$ $M_\odot$ pc^{-3} then is the present lower bound for the density that the central mass concentration must possess. Its half-mass radius is about $R_{1/2} = 0.01$ pc.

In addition, we note that the data in Fig. 8 *do not require* any additional component other than a point-mass (or a very compact dark cluster) plus an extended cluster of stars radiating at 2 μm. Such an additional component could be an *extended* dark mass, consisting of neutron stars, stellar black holes or white dwarfs (e.g. Morris 1993; Saha, Bicknell & McGregor 1996; Haller et al. 1996). However, considering the measurement uncertainties and the uncertainties in the core radius of the visible cluster, the data do not exclude any such extended dark mass either, as long as the cluster mass does not exceed ~ 3 to 6×10^5 $M_\odot$. If such an extended dark mass has a core radius similar to the visible cluster, its mass obviously could be yet greater.

3.4 Lower bound to the mass of Sgr A* itself

From a comparison of the stellar velocities near Sgr A* and an upper limit of the proper motion of the radio source itself, we can now derive a very significant lower limit to its mass. Backer (1996: see also Backer & Sramek 1982 and Backer 1994) has measured, with radio interferometry, the apparent proper motion of Sgr A* relative to three compact (extragalactic) radio sources that are at a separation of less than 1° from the Galactic Centre. The total proper motion of Sgr A* on the sky, $v_{\rm Sgr\,A^*}$, relative to an object at rest in the Galactic Centre, can then be inferred by subtracting the solar motion for a given Galactic Centre distance. There is no significant detection of any such intrinsic motion and Backer's most recent value (1996) for a Sun–Galactic Centre distance of 8 kpc is $v_{\rm Sgr\,A^*} \leq 16$ km s^{-1} (1σ). Unless the motion of Sgr A* happens to be very close to the line of sight its total velocity will be somewhat larger but comparable to this value. As the equipartition time-scale within the core radius of the stellar cluster is less than 10^7 yr for objects with masses greater than 10 $M_\odot$ (Genzel et al. 1994), it is plausible that Sgr A* has a similar kinetic energy to the stars in its vicinity. With this simple argument the mass of Sgr A* must be at least

$$m\,(\text{Sgr A*}) \geq \delta m_{\rm star} (v_{\rm star}/v_{\rm Sgr\,A^*})^2. \quad (5)$$

We have shown above that the Sgr A* cluster members likely are early-type stars of mass $m_{\rm star} = 15$ to 20 $M_\odot$. Taking the two-dimensional dispersion in the proper motions of the stars closest to Sgr A* (S1, S2, S3, S4 and S8) as a measure of $v_{\rm star}$ (~ 1150 km s^{-1}), we find that the mass of the compact radio source must be $\sim 10^5$ $M_\odot$. δ measures the deviation from equipartition. If equipartition is fulfilled $\delta = 1$, otherwise the velocity of Sgr A* is above the equipartition value and $\delta > 1$. *The mass of Sgr A* thus estimated exceeds, by orders of magnitude, anything that can be a stable star, neutron star or stellar black hole, and is a substantial fraction (≥ 5 per cent) of the total dark central mass in the Galactic Centre.* The diameter of the radio source Sgr A* is less than about 0.2 mas (2.4×10^{13} cm: Rogers et al. 1994; Krichbaum et al. 1994) and has been interpreted as the size of the hot plasma zone surrounding the central black hole (e.g. Melia, Jokipii & Narayanan 1992; Narayan, Yi & Mahadevan 1995). Hence the density of the mass associated with Sgr A* is likely greater than 3×10^{20} $M_\odot$ pc^{-3}. The upper limit to the radio radius of Sgr A* is only 15 times the Schwarzschild radius of a 2.6×10^6 $M_\odot$ black hole (7.8×10^{11} cm).

3.5 Mass-to-luminosity ratio for the dark mass

The possible infrared counterpart of Sgr A* (Fig. 1) has $m(K) \sim 15$ in 1996 June and > 16.3 in 1996 April. On average the luminosity of the dark central mass thus must be less than about 5×10^3 $L_\odot$ if it has a high temperature ($T \gg 6000$ K). Its mass-to-bolometric luminosity ratio thus is at least 25 if one takes the lower bound to the mass associated with the radio source as estimated in the last paragraph. If all of the dark mass is associated with the radio source the mass-to-luminosity ratio is 500 $M_\odot/L_\odot$ or greater. This excludes any known stellar aggregate consisting of normal stars more massive than 0.2 $M_\odot$. Leaving out speculative forms of matter, the dark mass – if it is not in the form of a single massive black hole – must either be an extremely dense, hard core cluster of stellar remnants (white dwarfs, neutron stars, stellar black holes) or of substellar entities (brown dwarfs, rocks).

3.6 Stability of a cluster with density $\geq 2 \times 10^{12}$ $M_\odot$ pc^{-3}

We now show from some fairly basic physical considerations that a dark mass concentration of 2.6×10^6 $M_\odot$, central density $\geq 2 \times 10^{12}$ $M_\odot$ pc^{-3} and half-mass radius ≤ 0.01 pc cannot be stable for more than 10^7 yr. A similar discussion can be found in Maoz (1995) in the context of the maser disc of NGC 4258. For a cluster of stars or stellar remnants with masses between 0.2 and 100 $M_\odot$ the evolution is determined by the relaxation time-scale t_{rh} through many long-range, weak gravitational interactions. This characteristic time-scale is given by the standard expression (Spitzer & Hart 1971; Binney & Tremaine 1987)

$$t_{rh} = 3.0 \times 10^5 \, (M_{2.6} R_{0.01}^3)^{0.5} m^{-1} [\ln (0.4\, M/m)/12]^{-1} \text{ (yrs)}. \quad (6)$$

Here, $R_{0.01}$ is the half-mass radius in units of 0.01 pc, $M_{2.6}$ is the dark mass in units of 2.6×10^6 $M_\odot$ and $m(M_\odot)$ is the mean mass of the cluster members. After t_{rh} the cluster approximately reaches a relaxed (thermal) state and after (10–16)t_{rh} the cluster experiences core collapse through binary formation and single–binary collisions with increasing hardening of the central binaries (see Binney & Tremaine 1987 and references therein). The subsequent evolution after initial core collapse depends on the composition and velocity dispersion of the cluster. Through gravitational wave losses a neutron star/black hole cluster of initial dispersion $\sigma \geq \sigma_{crit} \sim 500$ to 3000 km s^{-1} will experience global collapse within a Hubble time all the way to the relativistic final state of a single black hole (Zel'dovich & Podurets 1965; Shapiro & Teukolsky 1985; Goodman & Lee 1989). Extrapolating from the fast stars in the Sgr A* cluster, the dispersion of neutron stars or 10-$M_\odot$ black holes would be between 500 and 2000 km s^{-1} (depending on whether or not equipartition is fulfilled). Hence if the dark mass in the Galactic Centre were such a cluster it would be close to the critical density limit. For velocity dispersions smaller than σ_{crit} the dense, post-collapse cluster would experience a bounce, followed by a re-expansion. It is likely that during the dense collapse phase a central seed black hole is formed (e.g. Rees 1984; Lee 1995). The latter process would be especially efficient for stellar black holes, which can merge rapidly through gravitational radiation capture in close two-body encounters (Quinlan & Shapiro 1989; Lee 1995). After $\sim 1.5 \times 10^2 t_{rh}$, a significant fraction of the mass of the cluster would get lost through evaporation (Spitzer & Thuan 1972; Binney & Tremaine 1987). In the case of the Galactic Centre core collapse of the present dark cluster would happen in 4.5×10^5 yr for 10-$M_\odot$ black holes, 2.9×10^6 yr for 1.4-$M_\odot$ neutron stars and 6×10^6 yr for 0.6-$M_\odot$ white dwarfs. Evaporation would make such clusters unstable on 10 times that scale. All of these time-scales are extremely small compared with the total age of the Galactic nucleus. We conclude that a $> 2 \times 10^{12}$ $M_\odot$ pc^{-3} dark cluster cannot be a static configuration but would be extremely unstable to rapid collapse and dispersal. Lee (1995) has made Fokker–Planck calculations of the evolution of an $N \sim 10^{4...4.5}$ black hole cluster with initial density $\sim 10^6$ $M_\odot$ pc^{-3}. He finds that after initial core collapse the black hole cluster exhibits gravothermal oscillations on a time-scale of a few million years. In his calculations Lee does not consider seed black hole formation and growth. However, while the black hole cluster reaches peak densities during maximum core collapse approaching that measured in the Galactic Centre ($10^{11...12}$ $M_\odot$ pc^{-3}), the properties of the core-collapsed cluster are clearly very different from those seen near Sgr A*. The theoretical density distribution of the core-collapsed cluster is soft with $n(R) \sim R^{-2.2}$ and $\sigma(R) \sim R^{-0.1}$. The number of holes actually residing in the compact core is only a few tens. It follows that the dark mass in the Galactic Centre also cannot be explained as a particularly dense state of a dynamically evolving cluster of stellar remnants. In the case of neutron stars and white dwarfs an additional problem would be to understand how the core radius of the remnants can be so much smaller than that of the normal, solar mass stars with similar mass (the ratio of core radii is a factor of ≥ 60: see Genzel et al. 1996 for a more detailed discussion of this issue).

In the case of very low-mass stars and substellar remnants gravitational focusing can be neglected and the characteristic time-scale of evolution is given by direct two-body collisions on a time-scale (Binney & Tremaine 1987)

$$t_{coll} = (16 \pi^{1/2} n \sigma r^2)^{-1}. \quad (7)$$

Here, n is the number density of the dark objects, σ is again their one-dimensional velocity dispersion and r is the radius of the object. With the mass–radius (r) relation for brown dwarfs and other low-mass objects t_{coll} ranges between $\leq 10^2$ yr for $m = 10^{-6}$ $M_\odot$ and $\sim 10^6$ yr for $m = 0.1$ $M_\odot$ (Zapolsky & Salpeter 1969; Nelson, Rappaport & Joss 1986; Stevenson 1991). Hence a cluster of dark substellar remnants is also highly unstable and will collapse.

We conclude that there is no conceivable way that a $\geq 2 \times 10^{12}$ $M_\odot$ pc^{-3}, 2.6×10^6 $M_\odot$ dark cluster of stellar remnants or substellar entities can be stable over much longer than 10^6 to 10^7 yr. Given basic physical theory it appears thus unavoidable that a massive seed black hole has formed sometime in the past which then has grown slowly to its present mass by accretion of gas, stars or stellar remnants (Rees 1984).

3.7 Comparison to other dark central mass concentrations

The dynamic evidence for central mass concentrations in galactic nuclei has been growing enormously over the past decade or so. We refer to the recent review by Kormendy & Richstone (1995) for more detailed discussions and references to individual cases. The stellar kinematics in elliptical galaxies and central bulges (Bacon et al. 1994; Bender, Kormendy & Dehnen 1996; Kormendy et al. 1996a,b; van der Marel et al. 1994, 1997), the H_2O maser kinetics in the nearby LINER NGC 4258 (Greenhill et al. 1995; Myoshi et al. 1995) and the Hα kinematics in M87 (Ford et al. 1994; Harms et al. 1994) suggest the presence of central dark masses ranging from about 3×10^6 $M_\odot$ in M32 to 3×10^9 $M_\odot$ in M87. Fig. 9 summarizes the minimum inferred densities of the different cases. From this and the inferred mass-to-luminsoity ratios it is clear that almost all cases require unusually dense, and probably unrealistic concentrations of stellar remnants or very low-mass stars. M31 (Bacon et al. 1994) and M32 (van der Marel 1994, 1997; Bender et al. 1996) are at or above the limits of stable neutron star clus-

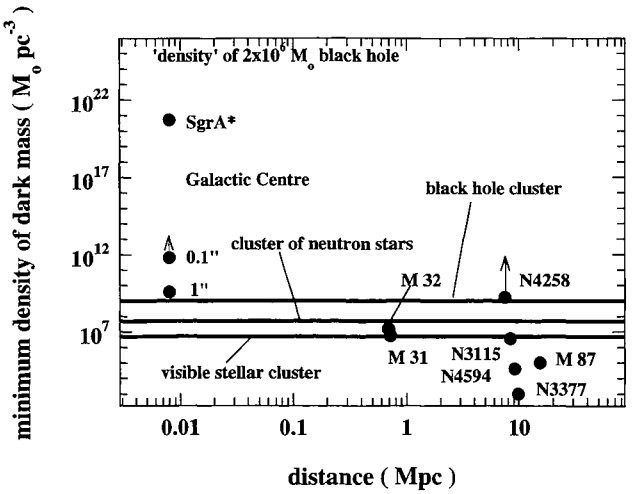

Figure 9. Comparison of inferred densities of dark central masses $[\rho(\mathrm{dark}) \sim M(\mathrm{dark})/4\pi R(\mathrm{min})^3/3]$ in a number of galactic nuclei (this paper; Bacon et al. 1994; Ford et al. 1994; Harms et al. 1994; van der Marel et al. 1994, 1997; Kormendy & Richstone 1995 and references therein; Myoshi et al. 1995; Kormendy et al. 1996a,b). The horizontal axis is the distance to the source. The equivalent density of a 2.6×10^6-$M_\odot$ black hole (within the volume defined by the Schwarzschild radius) is 4×10^{25} $M_\odot$ pc^{-3}. Indicated as horizontal lines are the maximum densities of various types of stable clusters (see text and references to theoretical work).

ters. The maser disc in NGC 4258 and the Galactic Centre stellar dynamics require dark mass concentrations well in excess of 10^9 $M_\odot$ pc^{-3}, which can only be explained by a compact cluster of stellar black holes or a single massive black hole. As Maoz (1995) has pointed out, the excellent fit of the maser velocities in NGC 4258 to a Kepler rotation curve together with the small velocity error bars allow a significant inward extrapolation of the required mass curve. Depending on how far inward this extrapolation can realistically be performed, the central density of the dark mass in NGC 4258 must be between 10^{11} and $10^{12.6}$ $M_\odot$ pc^{-3} (Maoz 1995), comparable to our estimate for the Galactic Centre. The discussion of the stability of dark clusters above has shown that stable dark clusters of neutron stars and stellar black holes at that density can be ruled out with some certainty. If one accepts these arguments it is hard to escape the conclusion that most of the dark mass in at least these two objects *must be in the form of a (single) massive black hole.*

ACKNOWLEDGMENTS

We thank the Director General and staff of ESO for their continuing support of our operation of SHARP at the NTT. N. Ageorges, R. Hofman, L. E. Tacconi-Garman and B. Sams have contributed to the construction of the SHARP camera and to a number of observing runs during various phases of this program. We are grateful to E. Becklin, A. Ghez, B. Klein and M. Morris for discussions on their first Keck observations of the Galactic Centre and to H. M. Lee for useful discussions on the stability of compact clusters. We appreciate the comments of G. Gilmore.

NOTE ADDED IN PROOF

New observations carried out in 1997 July using SHARP1 at the NTT have resulted in data that are fully consistent with the proper motions presented in this paper.

REFERENCES

Allen D. A., Hyland A. R., Hillier D. J., 1990, MNRAS, 244, 706
Backer D. C., 1994, in Genzel R., Harris A. I., eds, NATO ASI Series, The Nuclei of Normal Galaxies. Kluwer, Dordrecht, p. 403
Backer D. C., 1996, in Blitz L., Teuben P., eds, Unsolved Problems of the Milky Way. Kluwer, Dordrecht, p. 193
Backer D. C., Sramek R., 1982, ApJ, 260, 512
Bacon R., Emsellem E., Monnet G., Nieto J.-L., 1994, A&A, 281, 691
Bahcall J. N., Tremaine S. C., 1981, ApJ, 244, 805
Begelman M. C., Blandford R. D., Rees M. J., 1984, Rev. Mod. Phys., 56, 255
Bender R., Kormendy J., Dehnen W., 1996, ApJ, 464, L123
Binney J., Tremaine S., 1987, Galactic Dynamics. Princeton Univ. Press, Princeton, NJ
Biretta J. A., Lo K. Y., Young P. J., 1982, in Riegler G. R., Blandford R. D., eds, The Galactic Centre. Am. Inst. Phys., New York, p. 91
Christou J. C., 1991, Exp. Astron., 2, 27
Cohn H., 1980, ApJ, 242, 765
Eckart A., Genzel R., Krabbe A., Hofmann R., van der Werf P. P., Drapatz S., 1992, Nat, 355, 526
Eckart A., Genzel R., Hofmann R., Sams B. J., Tacconi-Garman L. E., 1993, ApJ, 407, L77
Eckart A., Genzel R., Hofmann R., Sams B. J., Tacconi-Garman L. E., Cruzalebes P., 1994, in Genzel R., Harris A. I., eds, NATO ASI Series, The Nuclei of Normal Galaxies. Kluwer, Dordrecht, p. 305
Eckart A., Genzel R., Hofmann R., Sams B. J., Tacconi-Garman L. E., 1995, ApJ, 445, L26
Eckart A., Genzel R., 1996, Nat, 383, 415 (EG)
Eckart A., Genzel R., 1997, MNRAS, 284, 576 (EG)
Ford H. C. et al., 1994, ApJ, 435, L27
Gatley I., Joyce R., Fowler A., DePoy D. L., Probst R., 1989, in Morris M., ed., The Centre of The Galaxy. Kluwer, Dordrecht, p. 361
Genzel R., Townes C. H., 1987, ARA&A, 25, 377
Genzel R., Hollenbach D. J., Townes C. H., 1994, Rep. Prog. Phys., 57, 417
Genzel R., Thatte N., Krabbe A., Kroker H., Tacconi-Garman L. E., 1996, ApJ, 472, 153
Goodman J., Lee H. M., 1989, ApJ, 337, 84
Greenhill L. et al., 1995, ApJ, 440, 619
Guesten R., Genzel R., Wright M. C. H., Jaffe D. T., Stutzki J., Harris A. I. 1987, ApJ, 318, 124
Haller J. W., Rieke M. J., Rieke G. H., Tamblyn P., Close L., Melia F., 1996, ApJ, 456, 194
Harms R. F. et al., 1994, ApJ, 435, L35
Hofmann R., Blietz M., Duhoux P., Eckart A., Krabbe A., Rotaciuc V., 1993, in Ulrich M.-H., ed., ESO Report 42, Progress in Telescope and Instrumentation Technologies. ESO, Garching, p. 617
Klein B. L., Ghez A. M., Morris M., Becklin E. E., 1996, in Gredel R., ed., ASP Conf. Ser. Vol. 102, The Galactic Centre. Astron. Soc. Pac., San Francisco, p. 228
Krabbe A., Genzel R., Drapatz S., Rotaciuc V., 1991, ApJ, 382, L19
Krabbe A. et al., 1995, ApJ, 447, L95
Kormendy J., Richstone D., 1995, ARA&A, 33, 581

Kormendy J. et al., 1996a, ApJ, 459, L57
Kormendy J. et al., 1996b, ApJ, 473, L91
Krichbaum T. P., Schalinski C. J., Witzel A., Standke K. J., Graham D. A., Zensus J. A., 1994, in Genzel R., Harris A. I., eds, The Nuclei of Normal Galaxies. Kluwer, Dordrecht, p. 411
Lacy J. H., Townes C. H., Geballe T. R., Hollenbach D. J., 1980, ApJ, 241, 132
Lee H. M., 1995, MNRAS, 272, 605
Lindqvist M., Habing H., Winnberg A., 1992, A&A, 259, 118
Lucy L. B., 1974, AJ, 79, 745
Maoz E., 1995, ApJ, 447, L91
McGinn M. T., Sellgren K., Becklin E. E., Hall D. N. B., 1989, ApJ, 338, 824
Melia F., Jokipii J. R., Narayanan A., 1992, ApJ, 395, L87
Menten K. M., Eckart A., Reid M. J., Genzel R., 1997, ApJ, 475, L111
Mezger P. G., Duschl W. J., Zylka R., 1996, A&AR, 7, 289
Morris M., 1993, ApJ, 408, 496
Myoshi M., Moran J. M., Hernstein J., Greenhill L., Nakai N., Diamond P., Inoue M., 1995, Nat, 373, 127
Narayan R., Yi I., Mahadevan R., 1995, Nat, 374, 623
Nelson L. A., Rappaport S. A., Joss P. C., 1986, ApJ, 311, 226
Osterbrock D. E., Miller J. S., 1989, Active Galactic Nuclei. Kluwer, Dordrecht
Quinlan G., Shapiro S. L., 1989, ApJ, 343, 725
Rees M., 1984, ARA&A, 22, 471
Reid M., 1993, ARA&A, 31, 345
Ricker G. R., Bautz M. W., DePoy D. L., Meyer S. S., 1992, in Riegler G. R., Blandford R. D., eds, The Galactic Centre. Am. Inst. Phys., New York, p. 97
Rieke G. H., Rieke M. J., 1988, ApJ, 330, L33
Rogers A. E. E. et al., 1994, ApJ, 434, L59
Rosa M. R., Zinnecker H., Moneti A., Melnick J., 1992, A&A, 257, 515
Saha P., Bicknell G. V., McGregor P. J., 1996, ApJ, 467, 636
Sellgren K., McGinn M. T., Becklin E. E., Hall D. N. B., 1990, ApJ, 359, 112
Serabyn E., Lacy J. H., 1985, ApJ, 293, 445
Shapiro S. L., Teukolsky S. A., 1985, ApJ, 292, L41
Spitzer L., Thuan T. X., 1972, ApJ, 175, 31
Spitzer L., Hart M. H., 1971, ApJ, 166, 483
Stevenson D. J., 1991, ARA&A, 29, 163
Storey J. W. V., 1982, in Riegler G. R., Blandford R. D., eds, The Galactic Centre. Am. Inst. Phys., New York, p. 85
Tanaka Y. et al., 1995, Nat, 375, 659
van der Marel R. P., Evans N. W., Rix H.-W., White D. D. M., De Zeeuw T., 1994, MNRAS, 271, 99
van der Marel R. P., de Zeeuw T., Rix H.-W., Quinlan G. D., 1997, Nat, 385, 610
Wollman E. R., Geballe T. R., Lacy J. H., Townes C. H., Rank D. M., 1977, ApJ, 218, L103
Zapolsky H. S., Salpeter E. E., 1969, ApJ, 158, 809
Zel'dovich Ya .B., Podurets M. A., 1965, SvA, 9, 752

APPENDIX A: COMMENTS ON INDIVIDUAL SOURCES NEAR Sgr A*

S1: this is the most significant high-velocity source in the northern part of the Sgr A* cluster. It is fairly well separated from other sources in its vicinity (S2, S3) and is apparent on all maps from 1992 to 1996. The elongated structure in our 0.15 arcsec map from 1996 June is due to a $\sim$0.5 to 1 mag fainter source located 0.1 arcsec north-east of S1 (Fig. 1, S12, see below).

S2 is strong and well separated from sources in the vicinity. Its inferred motion towards the south is strengthened by the 1992 data.

S3 is the faintest source in the northern part of the Sgr A* cluster that we have included in our analysis. The source is still recognizable in the 1996 June data. Because of its large inferred motion toward the north-east it is on the verge of being confused with with S1 and S2. The identification of S3 in our 1992 August image is difficult. In agreement with the backward extrapolation of the proper motions from 1994/1996, S3 and S9 are at that time close to and just north of S8. The combination of S3 and S9 probably accounted for most of the flux in the northern part of the north–south elongated source near S8 in 1992 August. It appears that S3 may be fading in 1996; its position in 1996 June may be affected by the new source, S12 (see below).

S4: in several of our best maps this source appears to have a companion approximately 0.1 arcsec to the north-east and about 2.5 mag fainter than the main component.

S5 is weak and confused with S4 and S6. In addition there is a weak source of about half its flux 0.15 arcsec north-east of it. For this reason S5 is given lower weight in our proper motion analysis.

S6/S7: both sources show the smallest proper motions in the Sgr A* cluster. S7 is about 1 mag fainter than S6 and just above the detection limit in the 1992 map.

S8/S9: S8 is currently the most isolated source in the cluster. Its fast motion to the east-southeast appears well established over all epochs. In 1996 it is clearly separated from S9, a weak source apparently rapidly moving south. S9 is difficult to locate in the 1992 map. In agreement with the 1994/1996 motion it probably was then just north of S8 (see comment on S3).

S10/S11: these bright sources in the southern part of the cluster form an apparent binary in projection. Although the change in position angle of the S10/S11 pair between 1992 and 1996 is one of the most prominent structural variations in the Sgr A* cluster, the exact proper motions of the two individual sources are hard to identify without ambiguity. In 1996 June, S10 is difficult to separate from S9 which is approaching from the north. Consistent with the backward extrapolation from 1994/1996, S10/11 were at similar positions in 1992. We also cannot exclude that the source structure contains additional fainter components. For all these reasons we have given these two sources lower weight in our proper motion analysis.

S12: this new source [$m(K) \sim 15$] appears between S1 and S3 in the super-resolved map obtained from all combined data sets taken in 1996 June (Fig. 1). It is clearly detected in all subsets of data during that epoch and causes the 'sausage' shape of S1 in Fig. 2. In 1996 April the super-resolved image in Fig. 1 shows no distinct source between S1 and S3. Any source at the position of S12 would have to be about $m(K) \sim 16.3$ or fainter. There is also no evidence for S12 on earlier data sets in Fig. 2. This strongly suggests that S12 is variable. Within the $\pm$30-mas uncertainties in relative positioning between the radio and the infrared frames, S12 is coincident with Sgr A*. S12 thus is the best present candidate for the infrared counterpart of the compact radio source. In order to confirm this finding the flux density and position of S12 need to be analysed in future epochs.